Relation between composition and fracture strength in off-stoichiometric metal silicide free-standing membranes

Shafikov, A.; van de Kruijs, R. W. E. ; Benschop, J. P. H.; Schurink, B.; van den Beld, W. T. E. ; Houweling, Z. S.; Kooi, B. J.; Ahmadi, M.; Graaf, S. de; Bijkerk, F.

Published in:
Intermetallics

DOI:
10.1016/j.intermet.2022.107531

Publication date:
2022

Intermetallics 144 (2022) 107531

Contents lists available at ScienceDirect

Intermetallics

journal homepage: www.elsevier.com/locate/intermet

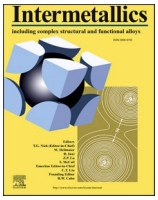

Relation between composition and fracture strength in off-stoichiometric metal silicide free-standing membranes

A. Shafikov [a,*], R.W.E. van de Kruijs [a], J.P.H. Benschop [a,b], B. Schurink [a], W.T.E. van den Beld [a], Z.S. Houweling [a,b], B.J. Kooi [c], M. Ahmadi [c], S. de Graaf [c], F. Bijkerk [a]

[a] Industrial Focus Group XUV Optics, MESA + Institute of Nanotechnology, University of Twente, Drienerlolaan 5, 7522 NB, Enschede, the Netherlands[1]
[b] ASML Netherlands B.V., Veldhoven, the Netherlands
[c] Zernike Institute for Advanced Materials, University of Groningen, the Netherlands

ARTICLE INFO

Keywords:
Intermetallics
Thin films and multilayers
Mechanical properties
Fracture
Microstructure
Electron microscopy
Transmission

ABSTRACT

In this work, we investigated the influence of composition on the polycrystalline structure, elastic properties and fracture strength, of Zr_xSi_{1-x}, Nb_xSi_{1-x}, and Mo_xSi_{1-x} free-standing thin films that were deposited by magnetron sputtering and subsequently annealed at 500 °C. Despite deviations from the stoichiometric composition, the crystalline structure of all films, except for the most Zr-rich Zr_xSi_{1-x}, corresponded to their respective stoichiometric disilicide structures, without the formation of a second-phase. Off-stoichiometry was found to be accompanied by the presence of lattice defects and a decrease of the grain size, which bring about a lower tensile stress in the films. The dependence of the fracture strength on the composition was remarkably similar for the three silicides, with the lowest and highest strength values occurring for samples with 30% and 37–40% of metal content, respectively. The observed dependence of strength on composition was attributed to the combination of the Hall-Petch effect, changes in the morphology and strength of grain boundaries, and the enhancement of crystal plasticity due to lattice defects induced by off-stoichiometry.

1. Introduction

Over the last few decades, refractory metal silicides received a lot of scientific interest due to their use in high-temperature applications. Their excellent high-temperature stability and mechanical properties make them interesting materials for heating elements, protective aerospace coatings, and other applications [1–4]. More recently, nanocrystalline metal silicide thin films, specifically $ZrSi_2$, $NbSi_2$, and $MoSi_2$, are being considered as candidates for the next generation of pellicle cores for extreme ultra-violet (EUV) lithography due to their high yield strength, thermal stability, metal-like emissivity, and high transmission in the EUV range [5]. An EUV pellicle is a thin film membrane, which is designed to protect the lithography mask from contamination during operation of the EUV lithography scanner. To allow for sufficient transmission of the EUV light, the EUV pellicle has to be extremely thin, just a few tens of nanometers. At the same time, the lateral dimension of the EUV pellicle is 7 orders of magnitude larger than the thickness: 11 cm × 14 cm [6]. Such extreme aspect ratio makes free-standing pellicles fragile and susceptible to mechanical disturbances during pellicle fabrication, handling, and operation of the EUV scanner. Hence, high strength and fracture resistance are some of the key requirements for an EUV pellicle.

EUV pellicles are subjected to a range of temperatures: from room temperature (during fabrication and handling) to several hundreds of degrees Celsius (during operation). At high temperatures metal silicides show good ductility, but at room temperatures they are brittle [7–10]. Dislocation slip is suppressed at low temperatures, therefore grains in polycrystalline metal silicides cannot undergo plastic deformation to relieve the microscopic stress concentrations that arise at the grain boundaries due to the elastic anisotropy of individual grains. As a consequence, grain boundaries, which have a lower atomic bond density compared to grains, act as the preferred sites for crack nucleation, which then results in a brittle fracture [11].

Studies on the improvement of low-temperature fracture properties of metal silicides have been primarily focused on alloying with other elements [10,12–14]. However, little attention has been paid to the

* Corresponding author.
E-mail address: a.shafikov@utwente.nl (A. Shafikov).
[1] www.utwente.nl/xuv

https://doi.org/10.1016/j.intermet.2022.107531
Received 11 October 2021; Received in revised form 4 March 2022; Accepted 7 March 2022
Available online 15 March 2022

effect of off-stoichiometry, i.e. a deviation of the atomic composition from the energetically most favourable composition. Similarly to alloying with a third element, small amounts of excess Me or Si atoms will lead to the formation of defects in the crystal lattice and therefore will have an impact on the mechanical properties of the material. Investigation of the influence of vacancies and antisites on the mechanical properties of metal silicides have been made in several theoretical studies [15–17]. The studies predict that the existence of such point defects in the crystal lattice should reduce shear resistance and enable room temperature crystal plasticity in silicides. Furthermore, deviations in the composition at the grain boundaries caused by segregation of excess atoms in off-stoichiometric material may affect their cohesive strength [18] and, as a result, the overall fracture strength of the material. Finally, the composition of the material will also affect its microstructure (grain size and grain boundary morphology), which play a big role in determining the mechanical properties.

Despite the potential for improvement of the fracture strength, no experimental studies have been conducted to investigate the effect off-stoichiometry in transition metal disilicides. Therefore, this work is aimed to find out, whether the Me/Si ratio can be used to control mechanical properties of polycrystalline metal disilicide thin films, namely $ZrSi_2$, $NbSi_2$, and $MoSi_2$, which are of high interest to EUV pellicle applications. For this, Me_xSi_{1-x} (Me = Zr, Nb, Mo) thin films with a varied composition (x in the range of 0.2–0.45) were prepared by magnetron sputtering, and their elastic properties and fracture strengths were investigated using a membrane bulge test. The mechanical properties are correlated with changes in microstructure, and likely strengthening/weakening mechanisms are discussed.

2. Experimental

2.1. Sample fabrication

In this work, mechanical properties of Me_xSi_{1-x} thin films are studied using membrane bulge testing performed on Si_3N_4/Me_xSi_{1-x} bilayer membranes. The steps of sample fabrication are illustrated in Fig. 1.

The process starts with the fabrication of single layer Si_3N_4 membranes using a standard silicon bulk micromachining process. A stoichiometric Si_3N_4 layer is grown by low-pressure chemical vapour deposition (LPCVD) at 750 °C on the back and the front side of a (100)-oriented 4-inch silicon substrate. After deposition, the Si_3N_4 layer on the backside of the substrate is patterned to expose the silicon substrate using UV lithography and reactive ion etch (RIE). The exposed silicon is then etched anisotropically in tetramethylammoniumhydroxide (TMAH) (25% solution in water) until free-standing Si_3N_4 windows are formed. The dimensions of the resulting free-standing membranes are 1 × 1 mm^2, with each membrane having a thickness of 25 nm, as determined by X-ray reflectometry (XRR). After the Si_3N_4 membranes are created, a metal silicide layer is deposited on the membranes by co-sputtering geometry using direct-current (DC) magnetron sputtering from Me (Zr, Nb, or Mo) and Si targets. Sputtering of Me_xSi_{1-x} layers was done using Ar gas at a pressure of about $7*10^{-4}$ mbar (gas flow rate of 27 sccm) with a background pressure of about $2*10^{-8}$ mbar. During deposition of the Me_xSi_{1-x} layer, the substrate (4-inch wafer with Si_3N_4 membranes) was kept stationary. This allowed to create a composition gradient in the Me_xSi_{1-x} layer over the substrate, as a result of Me and Si deposition rates decreasing with the distance to the respective magnetron target. The magnetron powers were chosen such that the composition varied around the $MeSi_2$ stoichiometry. As a result, depending on the location on the wafer, the value of x in the deposited Me_xSi_{1-x} layer was in the range from 0.2 to 0.25 to 0.4–0.45, as was verified by Rutherford backscattering spectrometry (RBS) done on the final samples (RBS data not shown here). Variation of x within each of the 1 × 1 mm^2 membranes was approximately 0.003, and 0.03 within the 10 × 10 mm^2 Si frames supporting each of the membranes. The deposited thicknesses for Me_xSi_{1-x} layers were in the range of 80–100 nm, as determined by XRR. To prevent oxidation of Me_xSi_{1-x} layers during thermal annealing, an approximately 10 nm thick SiN_x cap layer was deposited by reactive DC magnetron sputtering without breaking vacuum. For sputtering of SiN_x, an Ar + N_2 gas mixture with a base pressure of $7*10^{-4}$ mbar was used (22 sccm of Ar and 10 sccm of N_2). After deposition of the cap layer, the wafer was annealed in an atmospheric N_2 furnace at 500 °C for 2 h to induce crystallization of the Me_xSi_{1-x} layer. Finally, the protective SiN_x cap was removed by a low energy, 130 eV, Ar ion beam. This is done to ensure that the highest stress (which during bulge testing was located at the top surface of the membrane) and fracture will occur in the Me_xSi_{1-x}, and not in the SiN_x cap layer.

2.2. Structural characterization

The crystalline structure of the Me_xSi_{1-x} thin films was studied by Grazing Incidence X-ray Diffraction (GIXRD) using a Malvern Panalytical Empyrean diffractometer. To eliminate the background and the contribution from the underlying Si_3N_4 layer and Si frame, the signal measured on a single-layer Si_3N_4 membrane was subtracted from the signal from the bilayer Me_xSi_{1-x}/Si_3N_4 membranes. To estimate the size of the grains in the Me_xSi_{1-x} film from the GIXRD patterns, the Scherrer equation [19] was used:

$$d = \frac{K\lambda}{\beta cos\theta} \quad (1)$$

Where d is the coherence length, λ is the used wavelength, β is the full

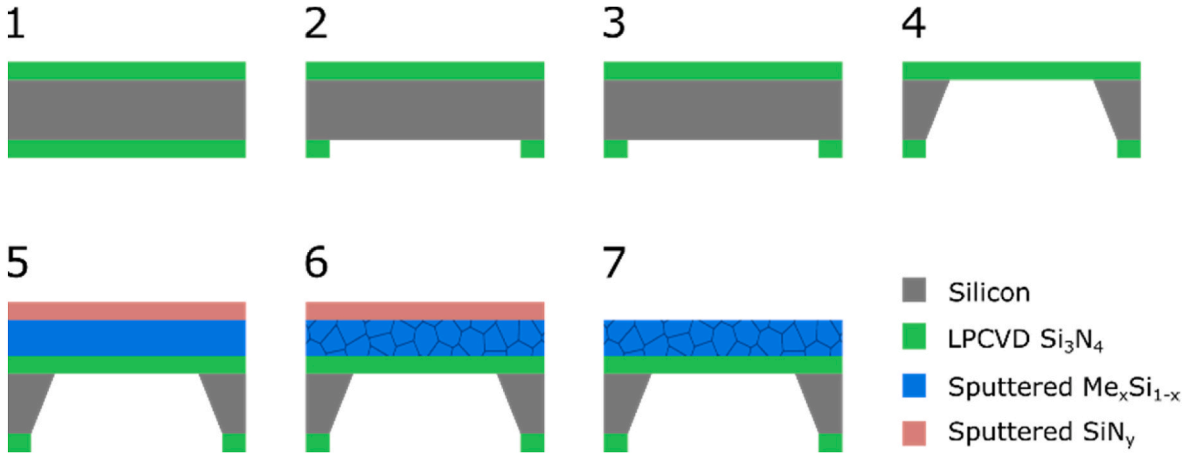

Fig. 1. Sample fabrication steps.

width at half maximum (FWHM) of the diffraction peak, K is the shape factor (typically close to 1), and θ is the Bragg angle. The coherence length can act as a reasonable estimate for the average grain size in the material (in the direction close to normal to surface, with the offset of θ), however, it is important to note that nano-strains and defects in the crystal lattice will also reduce the coherence length and increase the peak broadening, which may lead to an underestimation of the grain size using this equation. In addition, instrumental broadening must also be taken into account. In this work, we approximated the instrumental function of our XRD setup with a Gauss function with FWHM of 0.3°, which was predominantly caused by the 0.27° angular divergence of the parallel plate collimator. Assuming that the physical broadening of the XRD peaks is mostly caused by the size of grains, their profile can be expressed by a Lorentz function. Therefore to obtain the size broadening the XRD peaks were fitted with Voigt functions, which is a convolution of Lorentz and Gauss functions, with a fixed Gauss FWHM of 0.3°.

In addition to GIXRD, selected $Zr_{1-x}Si_x$ films were analyzed using Scanning Transmission Microscopy (STEM) recording images in High-Angle Annular Dark Field (HAADF) STEM mode and acquiring elemental maps using Energy Dispersive X-ray (EDX) spectroscopy, i.e. performing STEM spectrum imaging. For STEM a double aberration corrected and monochromated Thermo Fisher Scientific Themis Z operating at 300 kV was used, which is equipped with a Dual-X EDX system having a high collection efficiency with a solid angle of 1.76 srad. For the STEM studies, small 100 × 800–300 × 800 μm^2 membranes, supported on 3 × 3 mm^2 380 μm thick Si frames, were prepared using the same procedure as described in the previous section. To allow for better image resolution, the supporting Si_3N_4 membrane layer was removed and the Zr_xSi_{1-x} layers were thinned down using a low (130 eV) energy Ar beam, resulting in single layer Zr_xSi_{1-x} membranes with a thickness of approximately 60–80 nm.

2.3. Bulge testing

Mechanical properties of the Me_xSi_{1-x} and Si_3N_4 layers were studied using membrane bulge test method. In this method, a pressure difference is applied to the membrane, which causes the membrane to bulge and induces mechanical stress in it. By measuring the deflection of the membrane as a function of the applied pressure, one can extract the elastic properties of the layers, whereas burst pressure of the membrane can be used to determine fracture strength.

Fig. 2 shows a schematic of the bulge setup used in this work, which consisted of the membrane mounting stage, nitrogen gas supply with a pressure sensor, and a white light interferometer (WLI), which was used to record membrane deflection. To determine the elastic properties of the membrane layers, namely Young's modulus E and residual stress σ_0, membrane deflection h was measured as a function of the applied pressure P using WLI. For this, the membrane was mounted such that the pressure is applied from the cavity side (Fig. 2a), and the membrane deflection was determined as the height difference between the flat frame and the center of the membrane. The measured data was then fitted with the bulge equation for a square bi-layer membrane [20]:

$$P = 3.41 \sum_{n=1..2} \sigma_{0n} t_n \frac{h}{a^2} + \sum_{n=1...2} (1.981 - 0.585\nu_n) \frac{E_n}{1-\nu_n} t_n \frac{h^3}{a^4} \quad (2)$$

Where a is the half-width of the membrane window, t_n is the thickness and ν_n is the Poisson ratio of the n-th membrane layer. The fitting parameters, E_n and σ_{0n}, are Young's modulus and residual stress of the n-th layer.

After the elastic properties of the layers were determined, a bulge test was used to measure the fracture strength. For this, the samples were re-mounted on a bulge setup such that the pressure was applied to the flat side (Fig. 2b). This was done to ensure that membrane failure was caused by fracture of the Me_xSi_{1-x} layer and not the delamination at the interface between the Si_3N_4 layer and Si substrate. The value of applied pressure was then increased with a rate of roughly 1 kPa/s until the eventual burst of the membrane, which typically occurred in the range from 100 to 200 kPa. The measured value of burst pressure was then used to calculate fracture strength by finite element method (FEM) using the Comsol Multiphysics software package [21].

Fig. 3 presents an example of the calculated stress distribution in the membrane pressurized to the burst pressure (i.e. just before the fracture occurs) and a microscope image of one of the failed membranes. As one can see from the stress distribution shown in Fig. 3a, the highest stress is located at the edge of the membrane at the top surface of the Me_xSi_{1-x} layer and is several times higher than the stress in the free-standing part of the membrane. As a result, fractures originate in the Me_xSi_{1-x} layer, always very close to the middle of one of the four membrane edges. This was confirmed by the microscope images of the failed membranes. An example of such an image is given in Fig. 3b, which shows the residual membrane pieces attached to the frame pointing towards the fracture origin - the center of one of the four edges. Following the maximum stress criterion, commonly used for brittle materials, the fracture strength was determined as the max value of 1st principal stress in the Me_xSi_{1-x} layer.

3. Results

3.1. Structural characterization

To investigate the influence of the film composition on the nanocrystalline structure and elemental distribution in the Me_xSi_{1-x} films, the films were analyzed by XRD and STEM/EDX. The GIXRD patterns of the Me_xSi_{1-x} films are presented in Fig. 4. The GIXRD and omega scans (not given here) show that all the Me_xSi_{1-x} films have polycrystalline structures without preferential orientation. As can be seen from Fig. 4, all the diffraction peaks, except for the case of Zr_xSi_{1-x} with x > 0.4, can

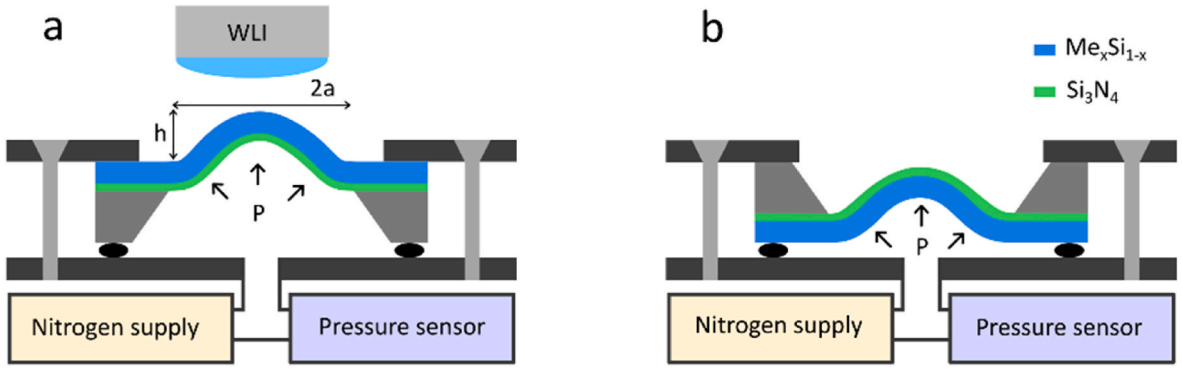

Fig. 2. Schematic of the bulge setup. (a) Configuration used during pressure-deflection measurements, pressure applied from cavity side; (b) configuration used during burst pressure measurements, pressure applied from the flat side of the membrane.

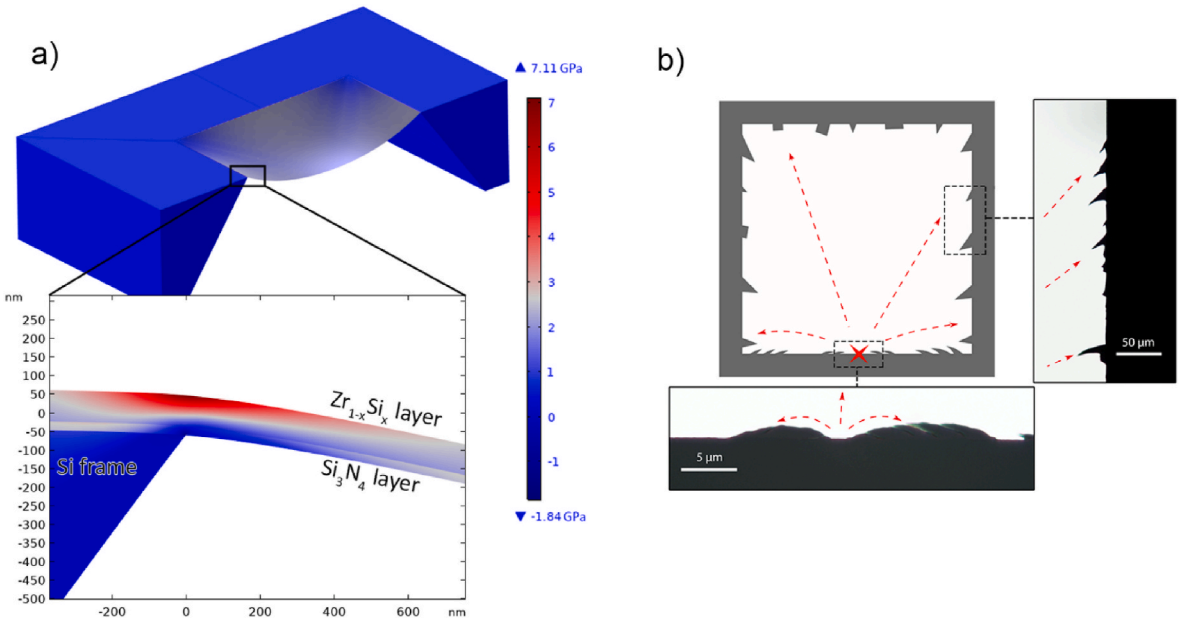

Fig. 3. (a) Stress distribution (1st principal stress) in a pressurized Zr_xSi_{1-x}/Si_3N_4 membrane calculated using FEM. Simulation parameters: $E_{Zr_xSi_{1-x}} = 170$ GPa, $E_{Si_3N_4} = 225$ GPa, $\nu_{Zr_xSi_{1-x}} = 0.2$, $\nu_{Si_3N_4} = 0.25$, $\sigma_{0Zr_xSi_{1-x}} = 720$ MPa, $\sigma_{0Si_3N_4} = 850$ MPa, $t_{Zr_xSi_{1-x}} = 85$ nm, $t_{Si_3N_4} = 24$ mm, $2a = 1.04$ mm, $P_{burst} = 142$ kPa. (b) Schematic and microscope images of a failed Zr_xSi_{1-x} membrane, showing the origin of fracture and the directions of crack propagation (indicated in red) inferred from the membrane residuals left on the frame.

be attributed to the respective $MeSi_2$ crystalline phase for each of the silicides: C49 $ZrSi_2$, C40 $MoSi_2$, and C40 $NbSi_2$. However, for compositions with $x < 0.4$, Zr_xSi_{1-x} films have a deviating crystal structure, which can be deduced from the disappearance of the C49 $ZrSi_2$ XRD peaks and simultaneous appearance of two pronounced new peaks at 28.5 and 37°. According to the Zr–Si phase diagram, the first stoichiometric phase with higher Zr content after $ZrSi_2$ is ZrSi. However, none of the three reported ZrSi structures (Bg, B33, B27) can explain the peaks observed for $x < 0.4$. Furthermore, to the best of our knowledge, none of the other reported Zr–Si structures match this XRD pattern [22,23]. For convenience, for the remainder of this work, we will refer to this unidentified phase as Zr_ySi_z. To determine the structure of the Zr_ySi_z phase, further thorough investigation and analysis of data is required, however, in the scope of this work, it is important to note that this change of the crystalline phase influences the mechanical properties of the film, as will be shown below in section 3.2.

Despite the deviations from the stoichiometric $MeSi_2$ compositions, in all cases, except $x > 0.4$ for Zr_xSi_{1-x}, no crystalline phases other than $MeSi_2$ were detected in the XRD patterns. At the same time, according to the equilibrium phase diagrams for these Me–Si systems, $MeSi_2$ phases are line compounds [23–25], which would suggest that the excess atoms should segregate towards amorphous grain boundary layers or clusters. To check the elemental distribution within the films, selected Zr_xSi_{1-x} samples were analyzed by STEM/EDX. Fig. 5 presents elemental maps obtained by STEM-EDX for three Zr_xSi_{1-x} samples with different compositions: $Zr_{0.25}Si_{0.75}$ (the most Si-rich), $Zr_{0.3}Si_{0.7}$, and $Zr_{0.36}Si_{0.64}$ (the most Zr-rich composition showing only $ZrSi_2$ peaks on the XRD pattern). Despite deviation from the stoichiometric $ZrSi_2$ composition, no considerable segregation of the excess Me or Si towards the grain boundaries was observed. Instead, the films showed a rather uniform distribution of the Zr/Si ratio. This suggests that the off-stoichiometric films exist in the metastable state, with the excess atoms being predominantly accommodated within the $MeSi_2$ lattice via defects, such as vacancies, antisites, or interstitials. This result is similar to the findings of Raaijmakers et al. [26], who investigated crystallization of $Ti_{0.3}Si_{0.7}$ (Si-rich) thin films and found that excess silicon remains inside the C49 $TiSi_2$ lattice upon crystallization if the annealing temperature stays below 750 °C, but starts precipitating at higher temperatures (with the amount of precipitates increasing with temperature).

While it is challenging to detect point defects (Si or Me vacancies, interstitials, or antisites which can be responsible for the off-stoichiometry of the crystal), other types of defects could be more easily observed in the HAADF-STEM images. Atomic resolution images, showing the existence of planar lattice defects in the off-stoichiometric Zr_xSi_{1-x} films, are given in Fig. 6a–b. Films with the most Si-rich composition ($Zr_{0.25}Si_{0.75}$) show an abundance of stacking faults when viewed along the (001) direction, as presented in Fig. 6a. Similarly, defects were found in the film with metal-rich composition. The image of the $Zr_{0.36}Si_{0.64}$ sample, given in Fig. 6b, shows stacking faults within grains, which result in the existence of multiple subgrain domains that have the same orientation but are displaced relative to each other. In comparison, analysis of the $Zr_{0.3}Si_{0.7}$ films could not confirm the existence of such defects, which indicates that their formation during crystallization requires a higher concentration of extra Si atoms. Still, the results suggest that higher concentrations of excess Si or Me atoms lead to a higher number of defects in the crystal lattice. To confirm this notion for the other films, which were not analyzed by TEM, we measured the change in the lattice constants using the XRD data. For this, we selected XRD peaks, which were sufficiently isolated from neighboring peaks and had high intensity, and fitted them with a Voigt function (as described in section 2.2). The peak positions obtained from the fitting and the values of residual stress in the film (results of stress measurements are given in section 3.2) were used to determine stress-free lattice constants. The obtained lattice constants are presented in Fig. 7a–c as a function of composition for the Zr_xSi_{1-x}, Mo_xSi_{1-x}, and Nb_xSi_{1-x} films. As one can see from the figures, a composition change is accompanied with a change in the lattice spacing in all three Me_xSi_{1-x} films, which confirms the existence of the defects resulting from off-stoichiometry. Interestingly, the lattice spacings are not a monotonous function of the composition. For values of x higher than approximately 0.3–0.33, an increase of Si content (and decrease of Me content) results in the contraction of the lattice. This is consistent with the results reported by Raaijmakers et al. [26], which show that the unit cell of $Ti_{0.3}Si_{0.7}$ expands with the increase of annealing temperature as a result of excess Si diffusing out of the lattice. However, for values of x lower than 0.3, an increase of Si content results in the expansion of the lattice

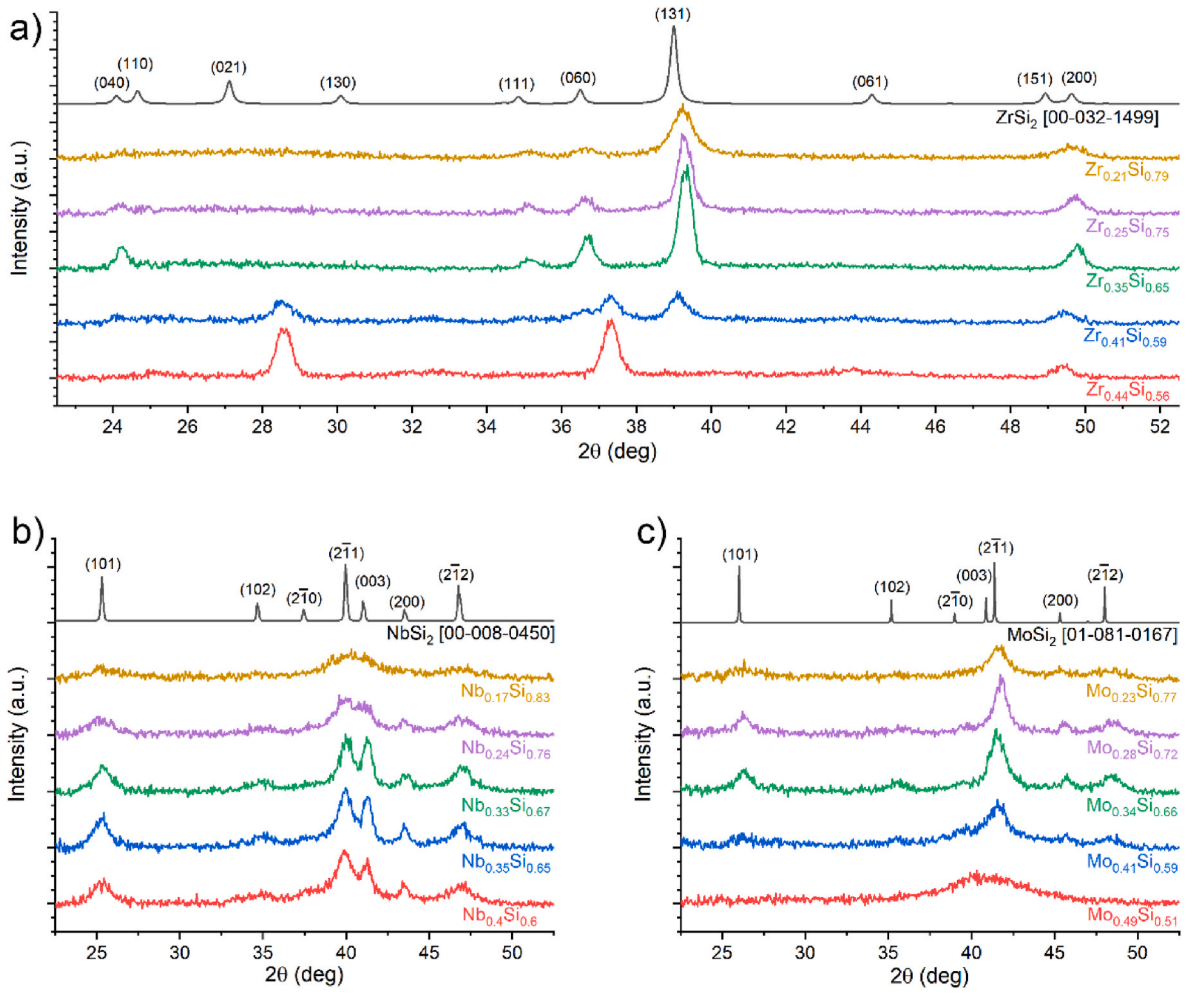

Fig. 4. Reference and measured GIXRD patterns for a) Zr_xSi_{1-x}, b) Nb_xSi_{1-x}, c) Mo_xSi_{1-x} layers. The signals are background corrected and normalized to the Me_xSi_{1-x} layer thickness.

(except for Nb_xSi_{1-x} shown in Fig. 7b, for which the peak positions could not be accurately determined due to the low intensity and large width of the peaks). This suggests that low concentrations of extra silicon are accommodated via Si_{Me} antisites or Mo vacancies (resulting in contraction), whereas at higher concentrations of Si, the excess atoms also occupy interstitial positions, resulting in the expansion of the lattice.

Apart from causing defects within the grains, off-stoichiometry was also found to affect the grain size and morphology of the grain boundaries, which also influence mechanical properties. Fig. 6c–e presents zoomed-out STEM images, which show the lateral polycrystalline structure in the analyzed Zr_xSi_{1-x} samples. As can be seen from Fig. 6e, the lateral size of the grains in the $Zr_{0.25}Si_{0.75}$ sample (Fig. 4e) is generally below 100 nm, which is considerably smaller than in the other two samples (Fig. 6c–d). The size of the grains in $Zr_{0.36}Si_{0.64}$ and $Zr_{0.3}Si_{0.7}$ is comparable to each other and reaches several hundreds of nm. However, there is a clear visual difference between these two samples. First, the grain interiors in $Zr_{0.36}Si_{0.64}$ have a more "cloudy" appearance, caused by the higher number of defects within the grains, as discussed earlier. Second, the morphology of the grain boundaries is different: while $Zr_{0.3}Si_{0.7}$ has relatively straight boundaries, in $Zr_{0.36}Si_{0.64}$ the boundaries, in general, are more irregular and zigzag-like. Such a zigzag-like structure can have an impact on the nucleation of cracks at the grain boundaries and will be discussed in section 4.1. To evaluate the influence of composition on the grain size in the other samples, which were not studied by STEM, we again analyzed the results of the XRD peak fitting, specifically peak broadening. Fig. 7d–f shows the Lorentz FWHM β of the fitted peaks and the corresponding coherence length d as a function of the film composition. The analysis shows that the increase of the excess Si or Me generally leads to the increase of peak broadening, i.e., that the grain size decreases as the composition becomes more off-stoichiometric. Note that for the most Mo-rich Mo_xSi_{1-x} ($x > 0.45$) XRD peaks could not be distinguished from the background due to significant broadening, which shows that the films are essentially amorphous. Interestingly, for Zr_xSi_{1-x} the smallest measured peak broadening does not correspond to $ZrSi_2$, but to a slightly silicon-rich composition $Zr_{0.31}Si_{0.69}$. Furthermore, in the case of Mo_xSi_{1-x} peak broadening appears to have a local maximum at the stoichiometric composition, with two minima corresponding to slightly Si-rich and Mo-rich compositions. However, it should be noted, that this behavior of the peak broadening might also be caused by factors other than grain size. For example, similarly to grain boundaries, lattice defects present within the grains will reduce the coherence scattering length and result in the increased broadening. Furthermore, the XRD signal is measured from a 1×1 cm^2 sample area (Si frame supporting the small 1×1 mm^2 membrane) over which there exists a gradient of composition (value of x varies by approximately 0.03). This, in combination with the change of lattice constants (i.e. peak position) with the change of composition, will also result in additional peak broadening. Still, the results of XRD measurements show that large deviations from stoichiometric composition lead to a reduction of the grain size in all three silicides. Again, this conclusion is in agreement with the study of crystallization of

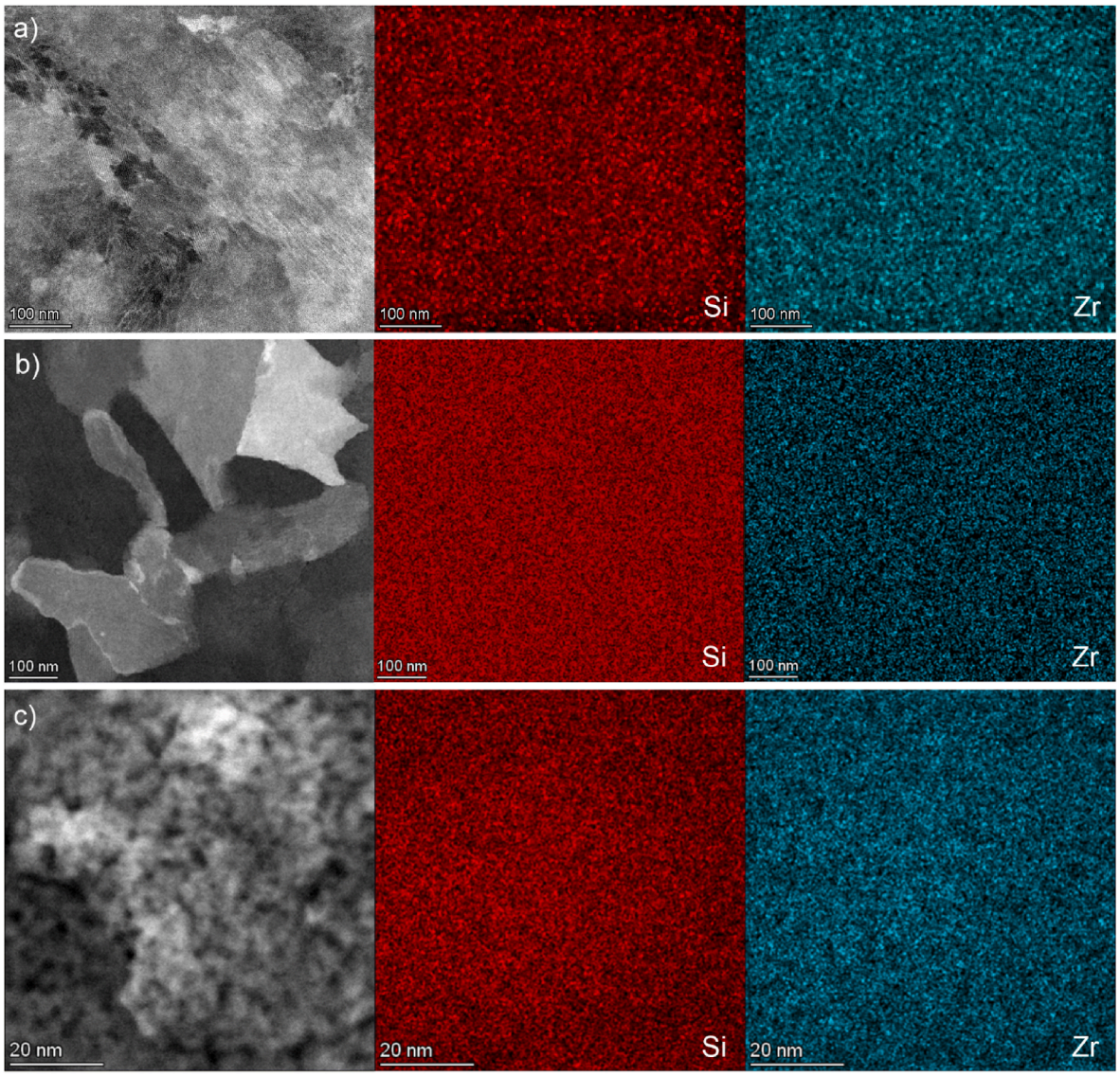

Fig. 5. STEM images of the areas analyzed by EDX and elemental maps showing the measured distribution of Si (red) and Zr (teal) in a) $Zr_{0.36}Si_{0.64}$, b) $Zr_{0.3}Si_{0.7}$ and c) $Zr_{0.25}Si_{0.75}$. Note: EDX maps are only used to characterize relative distribution of Zr and Si atoms due to the existing systematic errors in the analysis. The average values of x determined from STEM-EDX were about 5–7% lower than those obtained by RBS: 0.28, 0.25 and 0.20 for $Zr_{0.36}Si_{0.64}$, $Zr_{0.3}Si_{0.7}$ and $Zr_{0.25}Si_{0.75}$, respectively. This difference is believed to be caused primarily by a systematic error in the values of theoretical k-factors used in EDX analysis.

amorphous Ti_xSi_{1-x} [27], which shows that off-stoichiometry leads to a reduced rate of grain growth rates and, as a result, smaller grains.

To sum up, Me_xSi_{1-x} films have a polycrystalline structure with grains having the structure of the respective $MeSi_2$ phase (C49 $ZrSi_2$, C40 $NbSi_2$, and C40 $MoSi_2$) in all cases except for Zr_xSi_{1-x} with $x > 0.4$, which was found to crystallize into an unidentified Zr_ySi_z structure. Generally, deviation from the stoichiometric film composition was found to result in reduction of the grain size and formation of defects within the grains due to the need to accommodate the excess Si and Me atoms.

3.2. Bulge testing

The elastic properties of the layers were determined by the bulge test method, i.e., by measuring membrane deflection as a function of the applied pressure, and then fitting the data with equation (2). First, the residual stress σ_0 and Young's modulus E were determined for the Si_3N_4 layer by performing bulge tests on single layer 24 nm Si_3N_4 membranes. Assuming the Poisson ratio of Si_3N_4 to be $\nu^{Si_3N_4} = 0.25$ [28], the Young's modulus and the residual stress of Si_3N_4 were determined to be $E^{Si_3N_4} = 225 \pm 5$ GPa and $\sigma_0^{Si_3N_4} = 850 \pm 20$ GPa, respectively. After that, elastic properties of Me_xSi_{1-x} layers were determined by performing bulge tests on bilayer Si_3N_4/Me_xSi_{1-x} membranes. Since this conventional bulge test technique doesn't allow for simultaneous determination of Young's modulus E and Poisson ratio ν, values of Poisson ratio for $Me_{1-x}Si_x$ films were assumed constant and were taken from the literature: $\nu^{Mo_xSi_{1-x}} = 0.2$, $\nu^{Nb_xSi_{1-x}} = 0.18$, $\nu^{Zr_xSi_{1-x}} = 0.193$ [22,29,30].

The residual stress σ_0 of Me_xSi_{1-x} layers as a function of composition is presented in Fig. 8a. In all three silicides, σ_0 shows a maximum value at the $MeSi_2$ composition, and gradually reduces as the composition becomes more off-stoichiometric. In the case of Zr_xSi_{1-x}, as the composition becomes more metal-rich and x reaches the value of about 0.4, σ_0 increases again, which is related to the formation of the Zr_ySi_z crystalline phase. Such reduction of stress in the off-stoichiometric films is believed to be caused by two factors: a reduced size of the grains and an increased amount of lattice defects, which result in less efficient atomic packing. Fig. 8b presents values of Young's modulus E, which also shows similar trends for the three silicides. Starting with the most Si-rich composition, E gradually increases with the increase of Me content in all Me_xSi_{1-x}

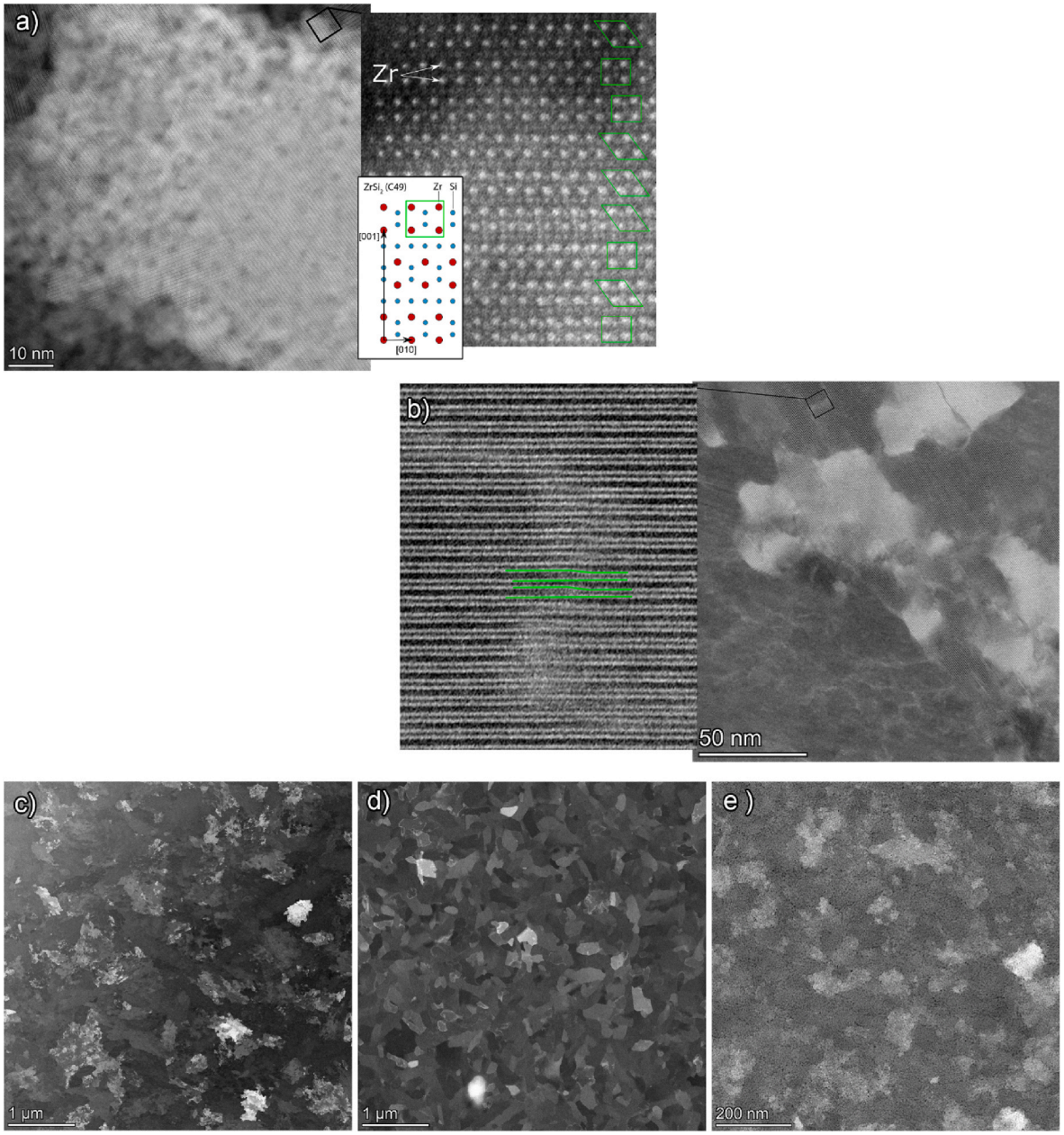

Fig. 6. Plan view HAADF-STEM images, showing stacking fault defects in a) $Zr_{0.25}Si_{0.75}$ and b) $Zr_{0.36}Si_{0.64}$ films (indicated by black arrows). Zoomed-out HAADF-STEM images of c) $Zr_{0.36}Si_{0.64}$, d) $Zr_{0.3}Si_{0.7}$, e) $Zr_{0.25}Si_{0.75}$.

films. However, after x reaches the value of around 0.4, further increase of Me content results in the decrease of E in Zr_xSi_{1-x} and Mo_xSi_{1-x}.

The results of fracture strength σ_f measurements are presented in Fig. 9. Starting with the most Si-rich composition, in all the three studied Me_xSi_{1-x} films, the increase of Me content leads to weakening in the region of x from 0.2 to 0.3. In the region around the stoichiometric $MeSi_2$ composition, x from 0.3 to approximately 0.36–0.4, the fracture strength goes up with increased content of Me. Finally, in the Me-rich region, where only Mo_xSi_{1-x} and Zr_xSi_{1-x} were tested, further increase of the Me content in the film again leads to strength weakening. Such striking similarity of the dependence of mechanical properties on composition between the three studied metal silicides suggests that the mechanisms behind the strength changes are the same between them, and may hold for other transition metal silicides.

4. Discussion

The results of the bulge test show that fracture strength is strongly influenced by the composition and structure of the $Me_{1-x}Si_x$ films. Since fracture of nano-crystalline materials involves multiple phenomena (such as plastic deformation of grains, grain boundary mediated plastic deformations, and eventual nucleation of nano-cracks at grain boundaries and triple [11,31,32]), there can be multiple mechanisms behind the observed change of fracture strength. In this section, we correlate the fracture properties to the polycrystalline structure and composition of the thin films, and discuss the likely mechanisms that cause the observed changes in fracture strength.

4.1. Bond strength and grain boundary morphology

Due to the lower density of bonds in comparison with the grain interiors, grain boundaries act as the weakest link in the fracture process.

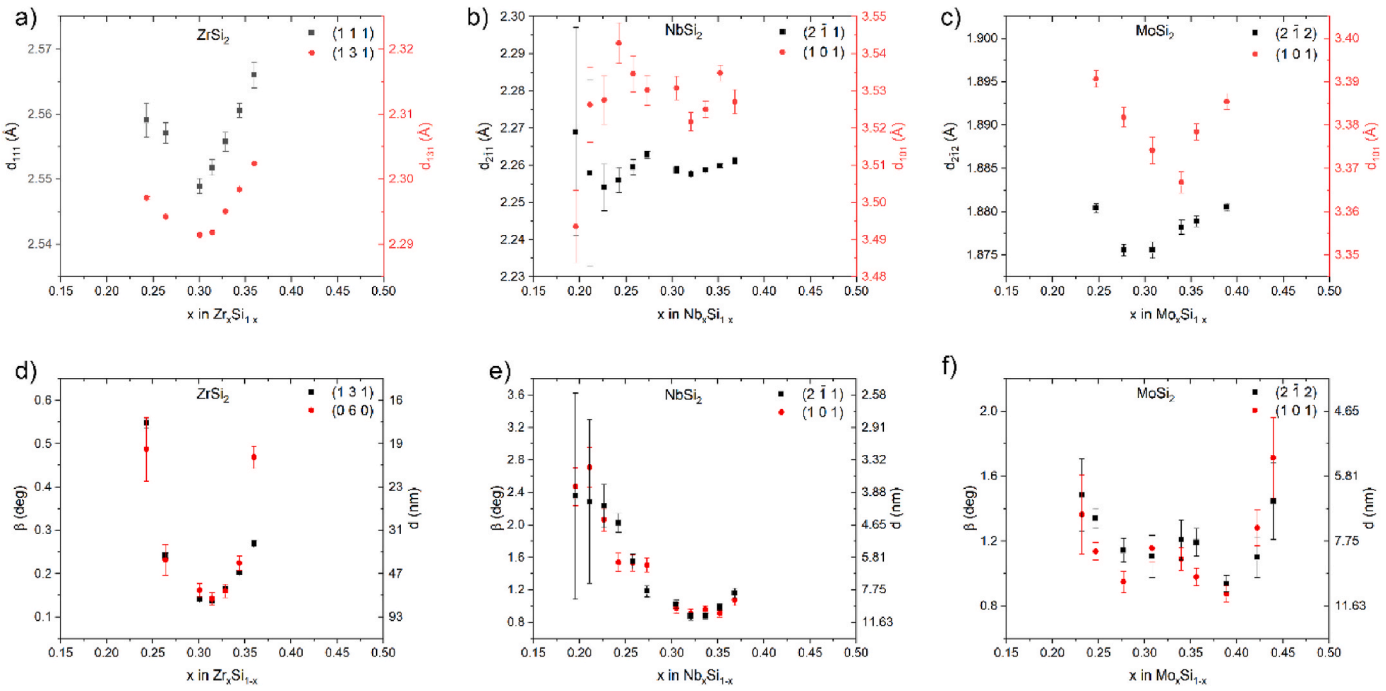

Fig. 7. a-c) Lattice spacings corresponding to XRD peaks films as a function of composition. d-f) Broadening of XRD peaks β as a function of film composition. The right Y-axis indicates coherence length d calculated from β using the Scherrer equation.

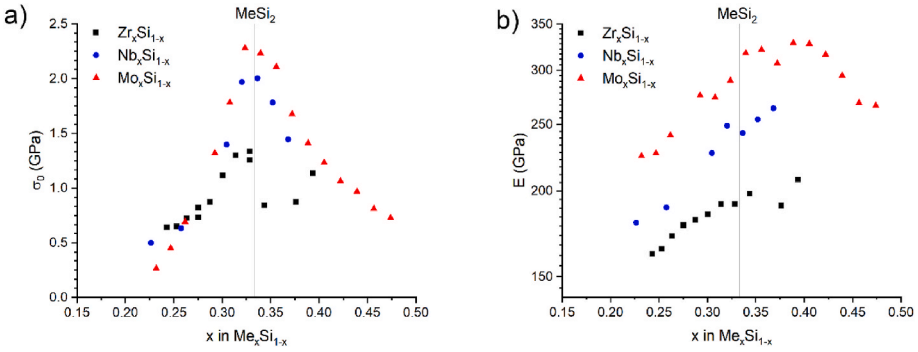

Fig. 8. a) Residual stress σ_0 and b) Young's modulus E of Me_xSi_{1-x} thin films as a function of film composition.

Therefore composition and morphology of the grain boundaries have a direct impact on the fracture strength of the material.

The results presented in section 3.1 indicate that majority of the excess Me and Si atoms are accommodated within the grains, rather than being segregated towards the grain boundaries or isolated clusters. Hence, the composition of the grain boundaries is likely to be close to the overall composition of the film. Still, this means that bonding at the boundaries will shift towards Me–Me in Me-rich films, and towards Si–Si in Si-rich ones. An ab initio theoretical study done by McMahan et al. [33] predicts the following bond strength hierarchy in Mo–Si compounds: Mo–Mo > Mo–Si > Si–Si. Assuming, that a similar trend holds for the other two silicides, we can expect an increase of average bond strength with the increase of metal content in the film. This notion is supported by the observed changes in Young's modulus, which is related to the theoretical strength of bonds as: $\sigma_{th} \cong \frac{E}{10}$ [34]. Indeed, in the range of x from 0.2 to 0.36–0.4 the elastic modulus of $Me_{1-x}Si_x$ films gradually increases as the metal content goes up. However, this effect cannot alone be responsible for the steep slope in the range of x between 0.3 and 0.36 (Fig. 9). While fracture strength increases by 30%–70% in that region, depending on the type of silicide, the expected change in the average theoretical strength of bonds is only about 10% (as estimated from the change of E in Fig. 8b). Furthermore, for $x < 0.3$, there exists a negative correlation between fracture strength and Young's modulus. Hence, the overall shape of the fracture strength curves is dominated by effects other than the one of bond strength.

It should be noted that an increase of metal content above 0.4 results in a reduction of the Young's modulus. For the Mo_xSi_{1-x} films, this is caused by the related dramatic drop in the size of the grains to the point when the structure can essentially be considered amorphous in the most Mo-rich films. A higher fraction of the grain boundaries in such fine-grained films leads to a lower overall density of bonds in the whole material and, as a result, a lower Young's modulus. The influence of the grains size and grain boundary volume fraction on strength will be discussed further, in section 4.3. In the Zr_xSi_{1-x} films, however, an increase of metal content above 0.4 does not lead to such dramatic reduction of grain size as in Mo_xSi_{1-x}, but rather to a change of the crystalline phase. Given that this change of the phase results in a lower Young's modulus, it can be argued that the reduced fracture strength of $Zr_{1-x}Si_x$ with $x > 0.4$ is explained by the lower theoretical strength of the Zr_ySi_z phase in comparison with the one of the $ZrSi_2$ phase.

Another important property that can influence fracture strength is the morphology of the grain boundaries. As argued in section 3.1,

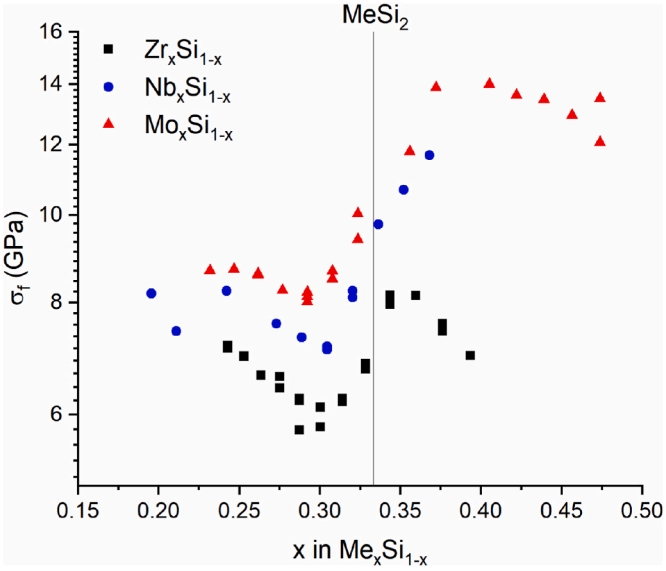

Fig. 9. Fracture strength of $Me_{1-x}Si_x$ thin films as a function of composition.

$Zr_{0.36}Si_{0.64}$ film shows irregular, zigzag-like grain boundaries, whereas the boundaries in $Zr_{0.3}Si_{0.7}$ are rather straight in comparison. Such a zigzag shape has been shown to have a positive effect on the strength of the grain boundaries [35,36]. The reason behind this strengthening effect is the increase in the resistance of grain boundaries to sliding. Therefore, nucleation and growth of nano-cracks at zigzag boundaries are hindered and require higher values of applied stress. Hence, we suggest, that the significant strengthening in the region of x between 0.3 and 0.37–0.4 can be explained by the increased irregularity of the grain boundaries.

4.2. Crystal plasticity

While fracture is expected to initiate from grain boundaries, rather than the interior of grains, the ability of grains to plastically deform can have a significant effect on the fracture process. Such deformations help to relax some of the stress that is accumulating at the grain boundaries, hindering the nucleation of cracks. Is known that, at room temperatures, metal disilicides have very limited plasticity due to the insufficient number of independent active slip systems in the crystal (according to the von Mises criterion, at least 5 slip systems are required for arbitrary plastic deformations). However, it has been experimentally shown that room temperature plasticity in metal silicides can be enhanced by alloying. For example, alloying with Nb, Ta, and Al was demonstrated to reduce hardness in C11b MoSi2 [10] single crystals, and alloying with Nb in particular allowed to observe room temperature ductility in polycrystalline $MoSi_2$ [8]. Similar to alloying, the existence of point defects in the lattice is also expected to assist plasticity, however, to the best of our knowledge, this has not yet been demonstrated experimentally. Using DFT calculations, Pan et al. [15,16] and Sun et al. [37] have predicted that in $MoSi_2$ and $NbSi_2$ lattice vacancies lead to an increase of the Pugh ratio (ratio between bulk modulus B and shear modulus G) and, as a consequence, are expected to improve plasticity [38]. Furthermore, crystal plasticity can be enabled by the stacking faults [39,40], which were observed in our films (Fig. 6a–c). This notion is in agreement with the results of this work: indeed, the fracture strength of both $Zr_{0.36}Si_{0.64}$ and $Zr_{0.25}Si_{0.75}$ films, which were found to contain stacking fault defects, is higher than the strength of $Zr_{0.3}Si_{0.7}$, in which such defects could not be found. However, it is reasonable to assume that a larger deviation from stoichiometric composition will result in an increased density of point defects and stacking faults within grains. Hence, one should expect a minimum or a change of the slope (given that defect density is not the only factor influencing strength) of the fracture strength graph (Fig. 9) near x = 0.33. The fact that the graphs for all three silicides are essentially linear in the interval between x = 0.3 and x = 0.36–0.4, suggests that the influence of point defects and grain plasticity on the fracture strength is not significant, and that fracture behavior is instead dominated by properties of the grain boundary network (i.e. grain size, morphology and composition of boundaries). However, to conclude this with certainty, other mechanical testing methods more suited for analyzing plastic behavior at the nano-scale need to be used.

4.3. Hall-Petch effect

The grain size is known to have an effect on strength of polycrystalline materials, which is described by the Hall-Petch relationship: $\sigma \sim d^{-0.5}$, where σ is the mechanical property related to strength (hardness, yield strength, fracture strength) and d is the characteristic size of grains. Depending on the exact material and failure mode, different physical mechanisms can be responsible for the Hall-Petch effect [41]. For the case of tensile fracture of a brittle material, the effect is explained by the differences in the volume fraction of the grain boundaries between the coarse and fine-grained materials. A larger volume fraction of grain boundaries in the material with smaller grains allows to accommodate a larger amount of plastic deformations within the grain boundary network before the eventual fracture, in other words, it essentially helps to spread the damage [42,43]. It can be argued, that the Hall-Petch effect has a dominant effect on the fracture strength of the Me_xSi_{1-x} films with $x < 0.3$. In this range, an increase in Si content (decrease of x) leads to a reduced grain size and, as a result, an enhanced fracture strength. However, the Hall-Petch effect is known to break down when grains size drops below some critical value, which typically is in the order of 10 nm. Below this value, reduction of grain size leads to weakening, which is known as the inverse Hall-Petch effect. This weakening can be attributed to the activation of grain boundary mediated plastic deformation mechanisms, such as grain boundary sliding and grain rotation [43]. In the present work, the inverse Hall-Petch effect appears to be responsible for the saturation of fracture strength observed in Nb_xSi_{1-x} and Mo_xSi_{1-x} for $x < 0.25$. Furthermore, the inverse Hall-Petch effect explains the weakening in Mo_xSi_{1-x} for $x > 0.4$, which occurs as the metal content is increased to the point where the films become essentially amorphous. By relating this strength weakening to coherence length determined from the width of XRD peaks, we can estimate that the critical grain size, below which inverse Hall-Petch becomes active, has to be higher than 6–7 nm. However, a more accurate estimation cannot be drawn from the data, since apart from the size of the grains, peak broadening is also contributed to by the existence of composition gradients over the sample and lattice defects.

5. Conclusions

In this work, the influence of deviations of metal disilicides from their standard stoichiometry due to their nanocrystalline structure, the elastic properties and fracture strength was systematically studied for Zr_xSi_{1-x}, Nb_xSi_{1-x}, and Mo_xSi_{1-x} films prepared by magnetron sputtering and annealed at 500 °C.

It was found that upon thermal annealing at 500 °C Me_xSi_{1-x} films form nanocrystalline structures without preferential grain orientation. All Me_xSi_{1-x} films, except Zr_xSi_{1-x} $x > 0.4$, crystallized into their respective $MeSi_2$ type structures: C49 for Zr_xSi_{1-x}, and C40 for Mo_xSi_{1-x} and Nb_xSi_{1-x}. The Zr_xSi_{1-x} films with $x > 0.4$ crystallized into an unknown Zr_ySi_z phase. Deviations from the stoichiometric composition resulted in reduced grain sizes and formation of lattice defects, which help to accommodate the extra Si and Me atoms in the off-stoichiometric films.

Residual stress was found to be lower in films with a larger deviation from stoichiometric composition, which is believed to be caused by less

efficient atomic packing due to the increased number of lattice defects and reduced grain size.

The fracture strength showed a very similar dependence on composition for the three studied silicides. The maximum strength corresponded to metal-rich compositions with a metal concentrations of approximately 37–40%, while the weakest films had compositions close to 30% metal. The observed dependence of strength on composition was concluded to be caused by a combination of the Hall-Petch effect (direct and inverse), changes in the morphology and strength of grain boundaries, and the enhancement of crystal plasticity due to lattice defects induced by off-stoichiometry. However, to get more quantitative information on the contributions of each of the strengthening/weakening mechanisms, further nanomechanical investigations need to be conducted. In particular, information about the amount and mechanisms of plastic deformations may provide a deeper understanding of how the fracture initiates in these nanocrystalline metal silicide films.

The results, presented in this article, demonstrate that the mechanical performance of metal silicide thin films can be improved by slightly deviating from stoichiometric $MeSi_2$ composition, in particular for Mo_xSi_{1-x} going from x = 0.33 to 0.37 results in a 40% increase of its fracture strength. Furthermore, off-stoichiometry also has the benefit of reducing residual stress in the films, which is an advantage for fabricating freestanding thin film membranes, because it lowers the risk of membrane failure under the residual tensile stress.

Author statement

A. Shafikov: Conceptualization, Investigation, Writing – original draft. **R.W.E. van de Kruijs**: Conceptualization, Supervision, Writing - review & editing. **J.P.H. Benschop**: Supervision, Writing - review & editing. **B. Schurink**: Investigation, Writing - review & editing. **W.T.E. van den Beld**: Investigation, Writing - review & editing. **Z.S. Houweling**: Supervision, Writing - review & editing. **B.J. Kooi**: Supervision, Writing - review & editing. **M. Ahmadi**: Investigation. **S. de Graaf**: Investigation. **F. Bijkerk**: Supervision, Funding acquisition, Writing - review & editing.

Declaration of competing interest

The authors declare that they have no known competing financial interests or personal relationships that could have appeared to influence the work reported in this paper.

Acknowledgements

This work is part of research programme of the Industrial Focus Group XUV Optics, being part of the MESA + Institute for Nanotechnology and the University of Twente, (www.utwente.nl/xuv) and the Industrial Partnership Programme “X-tools” (project No. 741.018.301). The work was financially supported by the Dutch Research Council (NWO), ASML, Carl Zeiss SMT, Malvern Panalytical and MESA+ institute.

References

[1] A.K. Vasudévan, J.J. Petrovic, A comparative overview of molybdenum disilicide composites, Mater. Sci. Eng. A. 155 (1992) 1–17, https://doi.org/10.1016/0921-5093(92)90308-N.
[2] J. Pelleg, Mechanical Properties of Silicon Based Compounds: silicides, 2019, https://doi.org/10.1007/978-3-030-22598-8.
[3] R. Mitra, Mechanical behaviour and oxidation resistance of structural silicides, Int. Mater. Rev. 51 (2006) 13–64, https://doi.org/10.1179/174328006X79454.
[4] S.P. Murarka, Silicide thin films and their applications in microelectronics, Intermetallics 3 (1995) 173–186, https://doi.org/10.1016/0966-9795(95)98929-3.
[5] P.J. van Zwol, M. Nasalevich, W.P. Voorthuijzen, E. Kurganova, A. Notenboom, D. Vles, M. Peter, W. Symens, A.J.M. (Jos) Giesbers, J.H. Klootwijk, R.W.E. van de Kruijs, W.J. van der Zande, P.J. van Zwol, M. Nasalevich, E. Kurganova, P. Voorthuijzen, D. Vles, M. Péter, W. Symens, W. van der Zande, A. Notenboom, J. H. Klootwijk, R.W. van de Kruijs, A.J.M. (Jos) Giesbers, Pellicle films supporting the ramp to HVM with EUV, Proc. SPIE 10451 (2017) 1–9, https://doi.org/10.1117/12.2280560.
[6] C. Zoldesi, K. Bal, B. Blum, G. Bock, D. Brouns, F. Dhalluin, N. Dziomkina, J.D. A. Espinoza, J. de Hoogh, S. Houweling, M. Jansen, M. Kamali, A. Kempa, R. Kox, R. de Kruif, J. Lima, Y. Liu, H. Meijer, H. Meiling, I. van Mil, M. Reijnen, L. Scaccabarozzi, D. Smith, B. Verbrugge, L. de Winters, X. Xiong, J. Zimmerman, Progress on EUV pellicle development, Extrem. Ultrav. Lithogr. 9048 (2014), https://doi.org/10.1117/12.2049276, 90481N.
[7] S. Nakatsuka, K. Kishida, H. Inui, Micropillar compression of MoSi2 single crystals, Mater. Res. Soc. Symp. Proc. 1760 (2015) 79–84, https://doi.org/10.1557/opl.2015.9.
[8] A.A. Sharif, A. Misra, T.E. Mitchell, Deformation mechanisms of polycrystalline MoSi2 alloyed with 1 at.% Nb, Mater. Sci. Eng. A. 358 (2003) 279–287, https://doi.org/10.1016/S0921-5093(03)00307-1.
[9] M. Moriwaki, K. Ito, H. Inui, M. Yamaguchi, Plastic deformation of single crystals of NbSi2 with the C40 structure, Mater. Sci. Eng. A. 239–240 (1997) 69–74, https://doi.org/10.1016/S0921-5093(97)00562-5.
[10] C. Zenk, J.S.K.L. Gibson, V. Maier-Kiener, S. Neumeier, M. Göken, S. Korte-Kerzel, Low temperature deformation of MoSi2 and the effect of Ta, Nb and Al as alloying elements, Acta Mater. 181 (2019) 385–398, https://doi.org/10.1016/j.actamat.2019.09.008.
[11] I.A. Ovid’ko, Review on the fracture processes in nanocrystalline materials, J. Mater. Sci. 42 (2007) 1694–1708, https://doi.org/10.1007/s10853-006-0968-9.
[12] A.A. Sharif, A. Misra, J.J. Petrovic, T.E. Mitchell, Alloying of MoSi2 for improved mechanical properties, Intermetallics 9 (2001) 869–873, https://doi.org/10.1016/S0966-9795(01)00084-X.
[13] A.A. Sharif, A. Misra, J.J. Petrovic, T.E. Mitchell, Solid solution hardening and softening in MoSi2 alloys, Scripta Mater. 44 (2001) 879–884, https://doi.org/10.1016/S1359-6462(00)00698-9.
[14] Y. Harada, Y. Murata, M. Morinaga, Solid solution softening and hardening in alloyed MoSi2, Intermetallics 6 (1998) 529–535, https://doi.org/10.1016/S0966-9795(97)00103-9.
[15] Y. Pan, J. Wang, D. Wang, H. Deng, Influence of vacancy on the elastic properties, ductility and electronic properties of hexagonal C40 MoSi2 from first-principles calculations, Vacuum 179 (2020), 109438, https://doi.org/10.1016/j.vacuum.2020.109438.
[16] Y. Pan, J. Zhang, C. Jin, X. Chen, Influence of vacancy on structural and elastic properties of NbSi2 from first-principles calculations, Mater. Des. 108 (2016) 13–18, https://doi.org/10.1016/j.matdes.2016.06.085.
[17] J. Chen, X. Zhang, D. Li, C. Liu, H. Ma, C. Ying, F. Wang, Insight into the vacancy effects on mechanical and electronic properties of Tantalum Silicide, Ceram. Int. 46 (2020) 4595–4601, https://doi.org/10.1016/j.ceramint.2019.10.189.
[18] A.I. Kovalev, D.L. Wainstein, A.Y. Rashkovskiy, Influence of Al grain boundaries segregations and La-doping on embrittlement of intermetallic NiAl, Appl. Surf. Sci. 354 (2015) 323–327, https://doi.org/10.1016/j.apsusc.2015.06.110.
[19] A.L. Patterson, The scherrer formula for X-ray particle size determination, Phys. Rev. 56 (1939) 978–982, https://doi.org/10.1103/PhysRev.56.978.
[20] R.J. Hohlfelder, Bulge and Blister Testing of Thin Films and Their Interfaces, Stanford University, 1999.
[21] The Structural Mechanics Module User’s Guide, COMSOL Multiphysics® V. 5.6, COMSOL AB, Stockholm, Sweden, 2020.
[22] S. Shu, F. Guo, Y. Zhan, Ab initio insight into the structure and properties of Zr–Si system, Phys. Status Solidi Basic Res. 256 (2019) 1–8, https://doi.org/10.1002/pssb.201900018.
[23] H. Okamoto, The Si-Zr (Silicon-Zirconium) system, Bull. Alloy Phase Diagrams 11 (1990) 513–519, https://doi.org/10.1007/BF02898272.
[24] H. Okamoto, Mo-Si (Molybdenum-Silicon), J. Phase Equilibria Diffus. 32 (2011) 176, https://doi.org/10.1007/s11669-010-9843-0.
[25] M.E. Schlesinger, H. Okamoto, A.B. Gokhale, R. Abbaschian, Errata: the Nb-Si (Niobium-Silicon) system, J. Phase Equil. 14 (1993) 541, https://doi.org/10.1007/BF02669132.
[26] I.J.M.M. Raaijmakers, A.H. Van Ommen, A.H. Reader, Crystallization of amorphous Ti-Si alloy thin films: microstructure and resistivity, J. Appl. Phys. 65 (1989) 3896–3906, https://doi.org/10.1063/1.343353.
[27] I.J.M.M. Raaijmakers, A.H. Reader, H.J.W. Van Houtum, Nucleation and growth of titanium silicide studied by in situ annealing in a transmission electron microscope, J. Appl. Phys. 61 (1987) 2527–2532, https://doi.org/10.1063/1.337928.
[28] J. Yang, O. Paul, Fracture properties of LPCVD silicon nitride thin films from the load-deflection of long membranes, Sens. Actuators A Phys. 97–98 (2002) 520–526, https://doi.org/10.1016/S0924-4247(02)00049-3.
[29] F. Chu, M. Lei, S.A. Maloy, T.E. Mrrchell, A. Migliori, J. Garrett, Single crystal elastic constants of nbsi2, Philos. Mag. B Phys. Condens. Matter; Stat. Mech. Electron. Opt. Magn. Prop. 71 (1995) 373–382, https://doi.org/10.1080/13642819508239040.
[30] J. Xu, J.D. Wu, D.H. Lai, Z.H. Xie, P. Munroe, Investigation on effect of alloying elements on mechanical properties of MoSi2 by first principle calculation, Mater. Sci. Technol. (United Kingdom) 28 (2012) 1337–1344, https://doi.org/10.1179/1743284712Y.0000000069.
[31] I.A. Ovid’ko, Micromechanics of fracturing in nanoceramics, Philos. Trans. A. Math. Phys. Eng. Sci. 373 (2015), https://doi.org/10.1098/rsta.2014.0129.
[32] G. Yang, S.J. Park, Deformation of single crystals, polycrystalline materials, and thin films: a review, Materials (Basel) 12 (2019), https://doi.org/10.3390/ma12122003.

[33] A.K. McMahan, J.E. Klepeis, M. Van Schilfgaarde, M. Methfessel, Bonding in the molybdenum silicides, Phys. Rev. B 50 (1994) 10742–10760, https://doi.org/10.1103/PhysRevB.50.10742.
[34] M. Friák, M. Šob, V. Vitek, Ab initio study of the ideal tensile strength and mechanical stability of transition-metal disilicides, Phys. Rev. B - Condens. Matter Mater. Phys. 68 (2003) 1–10, https://doi.org/10.1103/PhysRevB.68.184101.
[35] H.U. Hong, I.S. Kim, B.G. Choi, M.Y. Kim, C.Y. Jo, The effect of grain boundary serration on creep resistance in a wrought nickel-based superalloy, Mater. Sci. Eng. A. 517 (2009) 125–131, https://doi.org/10.1016/j.msea.2009.03.071.
[36] O. Miyagawa, M. Yamamoto, M. Kobayashi, Zig-zag grain boundaries and strength of heat resisting alloys, Superalloys, Met. Manuf, Proc Int Symp, 3rd (1976) 245–254, https://doi.org/10.7449/1976/superalloys_1976_245_254. Seven Springs.
[37] S.P. Sun, Y.F. Hu, X.P. Li, Y. Chen, H.J. Wang, Y. Yu, Y. Jiang, D.Q. Yi, The effect of point defect on mechanical properties of MoSi2, Int. J. Mod. Phys. B 31 (2017), https://doi.org/10.1142/S0217979217440817.
[38] S.F. Pugh, XCII. Relations between the elastic moduli and the plastic properties of polycrystalline pure metals, London, Edinburgh, Dublin Philos. Mag. J. Sci. 45 (1954) 823–843, https://doi.org/10.1080/14786440808520496.
[39] J. Li, J. Cho, J. Ding, H. Charalambous, S. Xue, H. Wang, X.L. Phuah, J. Jian, X. Wang, C. Ophus, T. Tsakalakos, R. Edwin García, A.K. Mukherjee, N. Bernstein, C. Stephen Hellberg, H. Wang, X. Zhang, Nanoscale stacking fault–assisted room temperature plasticity in flash-sintered TiO2, Sci. Adv. 5 (2019) 1–10, https://doi.org/10.1126/sciadv.aaw5519.
[40] D.G. Sangiovanni, W. Mellor, T. Harrington, K. Kaufmann, K. Vecchio, Enhancing plasticity in high-entropy refractory ceramics via tailoring valence electron concentration, Mater. Des. 209 (2021), https://doi.org/10.1016/j.matdes.2021.109932.
[41] Z.C. Cordero, B.E. Knight, C.A. Schuh, Six decades of the Hall–Petch effect – a survey of grain-size strengthening studies on pure metals, Int. Mater. Rev. 61 (2016) 495–512, https://doi.org/10.1080/09506608.2016.1191808.
[42] S. Gur, M.R. Sadat, G.N. Frantziskonis, S. Bringuier, L. Zhang, K. Muralidharan, The effect of grain-size on fracture of polycrystalline silicon carbide: a multiscale analysis using a molecular dynamics-peridynamics framework, Comput. Mater. Sci. 159 (2019) 341–348, https://doi.org/10.1016/j.commatsci.2018.12.038.
[43] H. Jia, X. Liu, Z. Li, S. Sun, M. Li, The effect of grain size on the deformation mechanisms and mechanical properties of polycrystalline TiN: a molecular dynamics study, Comput. Mater. Sci. 143 (2018) 189–194, https://doi.org/10.1016/j.commatsci.2017.10.054.